Soft Matter

Accepted Manuscript

ROYAL SOCIETY OF CHEMISTRY

www.rsc.org/softmatter

Journal Name

ARTICLE TYPE

Cite this: DOI: 10.1039/xxxxxxxxxx

Hydrodynamic interactions of deformable polymeric nanocarriers and the effect of crosslinking†

Arijit Sarkar,[a] David M. Eckmann,[b] Portonovo S. Ayyaswamy,[a] and Ravi Radhakrishnan*[c]

Received Date
Accepted Date

DOI: 10.1039/xxxxxxxxxx

www.rsc.org/journalname

We report theoretical as well as numerical investigations of deformable nanocarriers (NCs) under physiologically relevant flow conditions. Specifically, to model the deformable lysozyme-core/dextran-shell crosslinked polymer polymer-based NC with internal nanostructure and subject to external hydrodynamic shear, we have introduced a coarse-grained model for the NC and have adopted a Brownian dynamics framework, which incorporates hydrodynamic interactions, in order to describe the static and dynamic properties of the NC. In order to represent the fluidity of the polymer network in the dextran brush-like corona, we coarse-grain the structure of the NC based on the hypothesis that Brownian motion, polymer melt reptations, and crosslinking density dominate their structure and dynamics. In our model, we specify a crosslinking density and employ the simulated annealing protocol to mimic the experimental synthesis steps in order to obtain the appropriate internal structure of the core-shell polymer. We then compute the equilibrium as well as steady shear rheological properties as functions of the Péclet number and the crosslinking density, in presence of hydrodynamic interactions. We find that with increasing crosslinking, the stiffness of the nanocarrier increases, the radius of gyration decreases, and consequently the self-diffusivity increases. The nanocarrier under shear deforms and orients along the direction of the applied shear and we find that the orientation and deformation under shear are dependent on shear rate and the crosslinking density. We compare various dynamic properties of the NC as a function of the shear force, such as orientation, deformation, intrinsic stresses etc., with previously reported computational and experimental results of other model systems. The computational approach described here serves as a powerful tool for the rational design of NCs by taking both the physiological as well as the hydrodynamic environments into consideration. Development of such models is essential in order to gain useful insights that may be translated into the optimal design of NCs for diagnostic as well as targeted drug delivery applications.

1 Introduction

Targeting nanocarriers (NCs) loaded with drugs to specific pathological tissues in the body promises to improve the treatment and the early/correct detection of many diseases. Optimal targeting requires for the tuning of the physicochemical properties of the NCs in order to achieve the required pharmacodynamics[1–3]. In general, NCs can be classified into non-deformable (or hard) and deformable (or soft) categories. Non-deformable NCs are often made of a dense polymer matrix which undergoes erosion or swelling to release the drug. While the hardness gives the NC a definite shape and size which make it relatively easier to rationally account for physical effects such as hydrodynamic interactions, it is constraining because when functionalized, the targeting molecules (antibodies) are rigidly anchored providing very little compliance to facilitate multivalent binding interactions. Soft NCs, in contrast, deform under the application of external stress or when approaching a confining boundary, which can offer a larger area for adhesion (leading to an increased propensity for multivalent binding). However, deformable NCs are also typified by an enhancement in drug loss under high shear conditions in the vasculature, when the NC is away from the target site. Moreover, the irregular geometry of a deformed NC makes it not only difficult to account for the hydrodynamic interactions, but the deformability itself can impose entropic penalties which can severely compromise the propensity for multivalent binding interactions.

[a] Department of Mechanical Engineering and Applied Mechanics, University of Pennsylvania, Philadelphia, PA.
[b] Department of Anesthesiology and Critical Care, University of Pennsylvania, Philadelphia, PA.
[c] Department of Bioengineering, University of Pennsylvania, Philadelphia PA; E-mail: rradhak@seas.upenn.edu

The physical properties of the NC also directly impact their physiological performance. It has been shown that polystyrene-based (hard) NCs show a strong propensity for phagocytosis[4], which makes them amenable for easy capture by macrophages[5]. Altering the shape of these NCs can enhance their adhesion to the endothelium[6], however biocompatibility is usually a concern with such NC constructs. Micelles and related amphiphilic assemblies represent the smallest of the deformable NC constructs, but are typically faced with low drug encapsulation and low storage stability[7,8]. Liposomes are soft NCs, which offer a better control of size, and better drug encapsulation compared to their micellar counter-parts, but are typified by short shelf lives and high degrees of drug leakage[9]. In the deformable NC category, polymersomes offer a nice middle ground as they are mechanically robust and stable, and can fuse with cellular membranes to transfer cargo to cells[10]; however, in terms of biocompatibility, they leave more to be desired, as they can trigger pseudoallergic reactions due to the activation of the immune system. Other deformable NCs such as crosslinked polymers and polyvalent conjugates[11,12] promise control over size, rigidity, drug encapsulation, and storage stability[13,14], but their optimization in design is in the early stages. Although significant amount of research has been done on this topic, little has been achieved on the optimization of surface properties, payload capacity and other design concerns. Various combinatorial techniques, for functionalizing these constructs with ligands for diagnostic markers and encapsulation of drugs have opened new directions. However the lack of mechanistic understanding of how the nanostructure and dynamics of such NCs impact their pharmacokinetics has been a major impediment in their clinical translation, which is still in in vivo animal testing in terms of bench-to-bedside development[15].

In this article, we focus on a new class of biocompatible core-shell polymer-based NC consisting of a lysozyme rich core with dextran-rich corona, which has the capability to host small-molecule drugs as well as larger metal-oxide nanoparticles[11,16]. This unique architecture can be exploited in a range of biotechnology and biomedical applications involving diagnostic imaging and therapeutic delivery. However, its response to, and its performance in, the physiological environment remains to be quantitatively assessed, which currently limits its utility in rational design. In the aforementioned core-shell polymer construct, the lysozyme constitutes a defined central rigid core and the dextran brushes constitute a fluid and soft corona. The overall size of the NC assembly is tunable in the range of $100-500$ nm in diameter and is determined by the molecular weight of the dextran. The softness of the NC assembly is controlled by the degree of crosslinking interactions.

In previous studies in the literature which have focused on quantitative mechanisms applicable to NC interactions, the behavior of star like carriers has been modeled as multi-arm star shaped microstructures. Grest and Kremer[17], Grest *et al.*[18] have shown a way to compute microstructural conformations of star polymers at constant temperature using Langevin dynamics simulations. For large molecular weight of the polymer, i.e., for star-polymers with long arms, these authors[17,18] have computed static and dynamic properties such as structure factor, relaxation rates, and compared them with known results[19]. At time-scales larger than the inertial relaxation time, the free-draining fluid-like chain assumption made by these authors causes the frictional forces of all the arms of star polymer to be additive and to be equal to the frictional forces of isolated chain segments in the solvent. However, in general, due to solvent hydrodynamics, the frictional forces on the arms of the star polymer will be different when compared to isolated chain segments. Ripoll *et al.*[20] and Singh *et al.*[21] have introduced the effect of solvent hydrodynamics in calculating the dynamics of star shaped polymers using the multiple collision dynamics (MPC) model, while studying the effect of shear on the deformation of star-shaped microstructures. Similar treatments including hydrodynamic interactions but excluding inertial effects have been used to probe the effect of flow on microstructure deformation. For e.g., Foss and Brady[22], Hur *et al.*[23], Petera and Muthukumar[24] have characterized the gradual deformation of microstructures under weak flow conditions, and Schroeder *et al.*[25], Hsieh *et al.*[26], Jendrejack *et al.*[27] have considered the effect of hydrodynamic interactions under strong flow.

Most of the studies described above have focused on large ratios of end-to-end distances with respect to size of beads. In the core-shell cross-linked polymer[11], however, the length of the arms is on the same order as that of the core, such that their behavior will be less signified by self-entanglements within a chain/strand, while the crosslinking density will have a significant impact on the static and dynamic properties. In this limit, how precisely the internal hydrodynamics of the deformable NC relaxation is coupled to the external hydrodynamics, will determine core-shell polymer deformability, multivalent adhesion, and drug release kinetics, which will ultimately influence the efficacy and performance of these carriers in pharmacological and clinical settings[15]. For example, mixing of dextran brushes increases entropy, whereas crosslinking opposes the motion and imposes an entropic penalty. The shear stress near the endothelial surface in the microvasculature drives the system away from equilibrium (flow-free) conformations. Such hydrodynamic and thermodynamic constraints are explicitly captured in the coarse-grained model of the lysozyme-core/dextran-shell crosslinked star polymer model we have proposed here. We include stochastic and hydrodynamic shear forces to model the internal dynamics of these deformable carriers under physiologically relevant conditions. Brownian dynamics simulations are carried out to understand their equilibrium properties as well as the response to shear. We also include intra-particle hydrodynamic interactions[28] in order to resolve the internal relaxation of hydrodynamic modes and how they couple to the external flow-field. That is, depending on the inter-bead positions, radii, and the viscosity of solvent, this long-range interaction impacts the transient temporal response of the core-shell polymer. In Section 2 we describe the polymer configurations, in Section 3 we describe the simulation methodology, in Section 4 the static properties (including structure factors, radius of gyration) are computed as a function of crosslinking, and in Section 5 deformation and tumbling under shear are shown in terms of normal strain differences and shear strain. We also focus on extending this method to resolve the effect of inhomo-

geneity on intrinsic stresses, carrier deformation, and relaxation dynamics.

2 Core-Shell Cross-linked Polymer NC Model

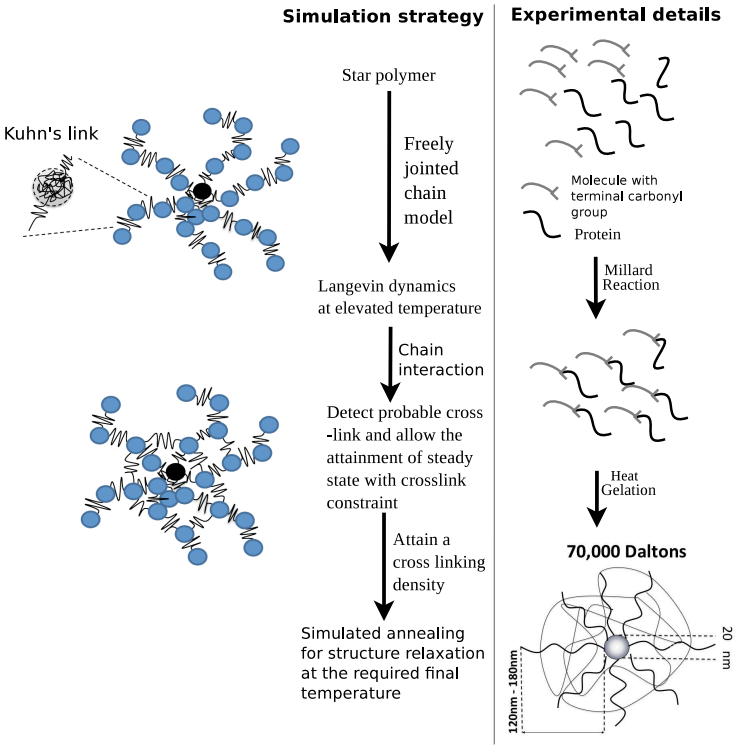

Fig. 1 Construction of the coarse-grained model for the core-shell polymer based NC and comparison with the experimental protocol.

We model the polymer microstructure as a fixed number of strands attached to a core, which mimics the experimentally inferred architecture for this material, see Figure 1, where each strand is modeled as connected segments of freely jointed chains (FJCs). The core radius is set to $a = 10$ nm following the experimental estimates of Coll Ferrer *et al.* [11,16]. For simplicity, we set the size of each bead in the arms to be the same as that of the core, i.e., $a = 10$ nm. The initial microstructure is a unit star polymer with 25 arms attached to a core, with each arm modeled by beads connected through four links in series; that is, each link connecting two adjacent beads in an arm is modeled as a Kuhn spring. Following Liu *et al.* [29], Pelton *et al.* [30], the stiffness of each link and the equilibrium distance is determined using a freely jointed chain model.

The molecular weight of a dextran monomer (denoted by M) is 162 Da[30]. For a typical molecular weight of 70 kDa of the dextran polymer used to synthesize the NC (see Figure 1), the number of monomers per arm is $\frac{70{,}000}{162}$ and the number of monomers per per bead is $N = \frac{70{,}000}{4\times 162}$. If the number of Kuhn's segments per bead is N_k and size of each Kuhn's segment is b_k, we impose $N_k b_k = Nb$, where b is the size of each monomer. For dextran, b_k is 0.44 nm[29] and the size of the monomer (b) is 1.5 nm using which we calculate the stiffness (k_s) of the links between beads as derived from the FJC model, i.e., $k_s = \frac{3k_BT}{N_k b_k^2}$. We also model the stiffness of the coarsegrained crosslinks to be identical to the stiffness of each link.

We mimic the experimental protocol to obtain a relaxed structure of the polymer assembly (see Figure 1): (1) we use molecular dynamics simulations to relax the structure at $1200K$. (2) At this high T, we track individual beads and the inter-bead distances between pair of beads from two different chains. If the center-to-center distance between beads is less than 19.7 nm – this is the distance from a given bead at which the probability to find a neighboring bead approaches zero, as evident from the radial distribution functions discussed below – , we assign a crosslink between the beads. (3) We repeat the crosslinking process for different pairs of beads until we reach the desired crosslinking density. (4) Once crosslinked, the interaction between beads is augmented by a harmonic potential. (6) We then follow a simulated annealing protocol described by Beers[31] in order to relax the crosslinked structure of the assembly to $300K$. For each crosslinking density we model $4-5$ configurations (replicas) and then carry out Brownian dynamics simulations as described equation (11) in each of the replicas. The error bars of the reported quantities are determined through the standard deviations of the five replicas.

3 Simulation Methodology

We solve the equations of motion of a system of connected beads in a solvent with the following parameters: the mass of each bead is m, the radius is a, the velocity is $\boldsymbol{v}$, the fluid viscosity is μ and fluid velocity is $\boldsymbol{v}_\infty$. The equations of motion for one bead are given by:

$$m\frac{\mathrm{d}\boldsymbol{v}}{\mathrm{d}t} + 6\pi\mu a\,(\boldsymbol{v}-\boldsymbol{v}_\infty) = \boldsymbol{F}_{br} + \boldsymbol{F}_{nbr}, \tag{1}$$

where F_{br} denotes Brownian forces and F_{nbr} denotes non-Brownian forces due to inter-bead interactions such as due to harmonic potentials constraining the beads and excluded volume interactions between beads. We consider time scales larger than the inertial relaxation time i.e., $t \gg \frac{m}{\xi}$, where $\xi = 6\pi\mu a$, for which, following Ermak and McCammon[32] we reduce equation (1) to:

$$\frac{\mathrm{d}\boldsymbol{r}}{\mathrm{d}t} = \boldsymbol{v}_\infty + M\,(\boldsymbol{F}_{br} + \boldsymbol{F}_{nbr})\,. \tag{2}$$

Here, for a given bead, $M = \frac{1}{\xi}$ is the mobility, and $\boldsymbol{r}$ is the position. We consider unconstrained Brownian forces as white noise which yields the following expressions:

$$\begin{aligned} \langle \boldsymbol{F}_{br}(t)\rangle &= \boldsymbol{0} \\ \langle \boldsymbol{F}_{br}(t)\boldsymbol{F}_{br}(t')\rangle &= 2k_BT\xi\delta(t-t')\boldsymbol{I}. \end{aligned}$$

Here, $\boldsymbol{I}$ is the unit second-order tensor, k_B is the Boltzmann constant, T is the temperature, and $\delta(t-t')$ is the Dirac delta function.

In addition to Brownian forces, the beads experience the following non-Brownian forces: (1) F^s represents the spring restoring forces derived from a harmonic potential between adjacent

connected beads:

$$U_s = \frac{1}{2}k_s\left(r - r_o\right)^2, \tag{3}$$

where r_o is the equilibrium bond distance, which is set to $2a$. Excluded volume interactions between beads is considered through the Weeks-Chandler-Anderson potential[33]:

$$U_{WCA} = 4\varepsilon\left[\left(\frac{\sigma}{r}\right)^{12} - \left(\frac{\sigma}{r}\right)^{6} + \frac{1}{4}\right], \tag{4}$$

for $r \leq r_C$ and $= 0$ for $r > r_C$; here, $\frac{\varepsilon}{k_BT}$ is the scaled interaction strength and σ is the excluded volume radius which we set to $\sigma = 2a$; the cut-off radius for the WCA potential is $r_C = 2^{1/6}\sigma$ and we set $\varepsilon = 0.7k_BT$.

So far, the equations of motion were described just for one bead. Below, we consider multiple beads and hydrodynamic interactions (HI) between two beads mediated by the solvent by adopting the Rotne–Prager–Yamakawa hydrodynamic mobility tensor[34,35] to introduce the effect of bead-to-bead hydrodynamics. For a pair of beads i and j, the pair-wise mobility is a function of configuration and is given by:

$$\begin{aligned}
&\boldsymbol{M}^{HI,ij} \\
&= \frac{1}{6\pi\mu a}\boldsymbol{I}\,, \text{ for } i = j \\
&= \frac{1}{8\pi\mu r}\left[\left(1 + \frac{2a^2}{3r^2}\right)\boldsymbol{I} + \left(1 - \frac{2a^2}{r^2}\right)\frac{\boldsymbol{rr}}{r^2}\right]\,, \text{ for } i \neq j, r \geqslant \sigma \\
&= \frac{1}{6\pi\mu a}\left[\left(1 - \frac{9r}{32a}\right)\boldsymbol{I} + \frac{3r}{32a}\frac{\boldsymbol{rr}}{r^2}\right]\,, \text{ for } i \neq j, r < \sigma,
\end{aligned} \tag{5}$$

where the superscript HI indicates hydrodynamic interactions, $\boldsymbol{r}^{ij} = \boldsymbol{r}$ is the relative position vector between bead i and j while $\boldsymbol{rr}/r^2$ is the product of normalized vectors. Since the mobility, formally valid at large separations, i.e., for $r \geqslant \sigma$, as shown in equation (5), decays slowly, (i.e., as $\frac{1}{r}$), the pairwise additive contribution of the hydrodynamic interaction term is still significant for interactions with the image beads of the periodic system, which is conceived as a 3D lattice system of identical cells of volume V; each image cell is denoted by an index $\boldsymbol{l}$ (see below) and contains the same number of beads N. We follow the Ewald summation method described by Beenakker[28] to account for the interactions from the periodic images. The resultant velocity is a product of the mobility resulting from the Ewald sum, and the forces acting on the bead, i.e.:

$$\boldsymbol{v}^i = \sum_{j=1}^{N}\sum_{\boldsymbol{l}}\boldsymbol{M}^{HI,ij}\left(\boldsymbol{r}_{\boldsymbol{l}}^{ij}\right)\cdot\boldsymbol{F}^j, \tag{6}$$

where $\boldsymbol{r}_{\boldsymbol{l}}^{ij}$ is the distance between bead i in the central simulation box and bead j in the image replica indexed by $\boldsymbol{l}$, which is comprised by the components of the 3D lattice vector expressed as $\boldsymbol{l} = (l_1L, l_2L, l_3L)$ and L is the length of the simulation box. The central simulation box is given by $\boldsymbol{l} = 0$ and the distance between bead i and bead j in the central box is therefore $\boldsymbol{r}_{\boldsymbol{l}=0}^{ij}$ which for simplicity is just denoted by $\boldsymbol{r}^{ij}$; with this simplification in notation, $\boldsymbol{r}_{\boldsymbol{l}}^{ij} = \boldsymbol{r}^{ij} + \boldsymbol{l}$. The mobility term for $r < \sigma$, does not contribute to the long-ranged hydrodynamic interaction, and hence it is added separately only for $\boldsymbol{l} = 0$. These, considerations collectively lead to the relationship:

$$\begin{aligned}
6\pi\mu a\boldsymbol{v}^i &= 6\pi\mu a\sum_{j=1}^{N}\boldsymbol{M}^{HI,ij}\left(\boldsymbol{r}^{ij}\right)\cdot\boldsymbol{F}^j \\
&+ \left(-6\frac{\zeta a}{\sqrt{\pi}} + \frac{40}{3}\frac{\zeta^3a^3}{\sqrt{\pi}}\right)\boldsymbol{F}^i \\
&+ \sum_{\substack{\boldsymbol{l}\\(\boldsymbol{l}\neq 0)}}\sum_{j=1}^{N}\boldsymbol{M}^{(1)}\left(\boldsymbol{r}^{ij} + \boldsymbol{l}\right).\boldsymbol{F}^j \\
&+ \frac{1}{V}\sum_{\substack{\boldsymbol{k}\\\boldsymbol{k}\neq\boldsymbol{0}}}\sum_{j=1}^{N}\boldsymbol{M}^{(2)}\left(\boldsymbol{k}\right)\cos\left(\boldsymbol{k}\cdot\boldsymbol{r}^{ij}\right).\boldsymbol{F}^j.
\end{aligned} \tag{7}$$

equation (7) defines the pair-wise mobility $\boldsymbol{M}^{ij}$, which includes hydrodynamic interactions and contribution from image-replicas:

$$6\pi\mu a\boldsymbol{v}^i = 6\pi\mu a\sum_{j=1}^{N}\boldsymbol{M}^{ij}\left(\boldsymbol{r}^{ij}\right)\cdot\boldsymbol{F}^j. \tag{8}$$

Here, $\boldsymbol{M}^{(1)}$ and $\boldsymbol{M}^{(2)}$ are functions of the inter-bead distance, derived by Beenakker[28]. The lattice sum over $\boldsymbol{M}^{(2)}$ is in reciprocal space over reciprocal lattice vectors $\boldsymbol{k}$, where $\boldsymbol{k} = 2\pi\boldsymbol{M}/L$, and $\boldsymbol{m} = (m_1, m_2, m_3)$, which all take integer values. We check for the convergence of the mobility tensor in determining the number of lattice vectors, k-points, and to justify the value of ζ; specifically, we use $125 - 216$ k-points, 27-125 lattice vectors, and set $\zeta = \sqrt{\pi}V^{-1/3}$. The sum mentioned in equation (7) is only for valid $r > 2a$, and hence, to introduce the effect of overlapping beads, the term shown in equation (5) for $r < 2a$ is added to keep the Rotne-Prager-Yamakawa tensor ($\boldsymbol{M}^{ij}$) positive-definite for all configurations[36]. Since, the term associated with $r < 2a$ does not contribute to the long-ranged part of the Rotne–Prager–Yamakawa tensor (i.e., it only survives for $n = 0$), it is kept out of the real space lattice sum, and is added outside the sum.

The resulting equations of motion are given by:

$$\frac{\mathrm{d}\boldsymbol{r}^i}{\mathrm{d}t} = \boldsymbol{v}_\infty + \sum_{j=1}^{N}\boldsymbol{M}^{ij}\cdot\left(\boldsymbol{F}_{WCA}^j + \boldsymbol{F}_s^j\right) + \sqrt{2}\sum_{j=1}^{N}\boldsymbol{B}^{ij}\cdot\boldsymbol{n}^j. \tag{9}$$

Here, $\boldsymbol{B}$ is a weight factor and $\boldsymbol{n}$ is a random vector chosen from a Gaussian distribution of zero mean and unit variance. $\boldsymbol{B}$ is computed by the domain decomposition of $\boldsymbol{M}$, i.e.,

$$\boldsymbol{M} = \boldsymbol{B}\cdot\boldsymbol{B}^T. \tag{10}$$

We follow the Cholesky decomposition for the domain decomposition of the Rotne–Prager–Yamakawa tensor.

We scale time t with the relaxation time of diffusion $\frac{a^2}{D_o}$ (where D_o is the unconstrained diffusivity of a Brownian bead given by $\frac{k_BT}{\xi}$), we scale r with a, M is scaled by $\frac{D_o}{k_BT}$, and F with $\frac{k_BT}{a}$. We use a nondimensional form of the spring energy, in terms of $\bar{k} = \frac{ka^2}{k_BT}$, which is a non-dimensionalized stiffness constant. In general, we

use an over-bar to signify the non-dimensionalized form of the parent variable. We rewrite equation (9) in-terms of scaled variables to yield:

$$\frac{\mathrm{d}\bar{\boldsymbol{r}}^i}{\mathrm{d}\bar{t}} = Pe + \sum_{j=1}^{N} \bar{\boldsymbol{M}}^{ij} \cdot \left(\bar{\mathbf{F}}^j_{WCA} + \bar{\mathbf{F}}^j_s\right) + \sqrt{2}\sum_{j=1}^{N} \bar{\boldsymbol{B}}^{ij} \cdot \mathbf{n}^j. \qquad (11)$$

Here, Pe is the Péclet number($\frac{v_\infty a}{D_o}$) and the overbar is used to represent the scaled variables. We use the forward explicit Euler time integration method to discretize equation (11) and solve for the time evolution of the positions of the beads. We use viscosity of the blood plasma (μ) as 1.3mPa.s., and the temperature T as $300K$.

For the WCA potential, the inertial time τ_{WCA} is $\sigma\sqrt{\frac{m}{\epsilon}}$ (where, m is the mass of a bead), while for Brownian dynamics, the time scale (τ_{Br}) is $\frac{a^2}{D_o}$. We find that for our system: $\frac{\tau_{WCA}}{\tau_{Br}} \approx 1.1 \times 10^{-3}$. We note that one can estimate the collisional time for WCA particles in the condensed phase based on an effective thermodynamic potential given by $-k_B T \ln g(r)$, where $g(r)$ is the radial distribution function introduced below; we find that the estimate for the collisional time is larger than τ_{WCA}.

The value of the time step of integration we use ranges from $10^{-5} - 5 \times 10^{-7} \frac{a^2}{D_o}$, which is (much) smaller than both τ_{WCA} and τ_{Br}, hence easily satisfies the linear stability criterion. The initial configuration (generated by the simulated annealing protocol) is allowed to equilibriate for $1 \times 10^4 - 1 \times 10^6$ time steps; we note below that this length of time exceeds the slowest timescales of relaxation typical for our systems, thereby ensuring equilibrium.

The configurations are then subjected to Brownian dynamics simulations. Following Grest *et al.* [42] for 0% crosslink NC, the largest relaxation time is $23.8\frac{a^2}{D_o}$. NC with large degree of crosslinking will relax like a hard sphere of equivalent radius of gyration, and the corresponding relaxation rate is smaller than that for star polymers. We first simulate the production runs for $25\frac{a^2}{D_o}$. We save the last configuration, which is then used as the initial configuration for the next simulation run, which is executed for a period of $25 - 50\frac{a^2}{D_o}$. For each configuration (replica), we perform atleast 3 independent simulations with different initial conditions. We the repeat these steps for $4 - 5$ independent configurations (replicas with varying internal structures). The procedure for estimating the statistical error is based on computing the standard deviation across these replicas, as noted earlier.

Overall the position vectors of beads are recorded for $2.5 \times 10^6 - 5 \times 10^7$ time steps. The computations for a typical trajectory noted above require 4 CPU-weeks on a single core of an Intel Xeon 2.7 GHz workstation.

4 Static Properties: Results and Discussion

4.1 Radial distribution function

The radial distribution function quantifies spatial variance of density of beads and it is defined as:

$$g(r) = \frac{1}{N\rho}\left\langle \sum_{i}^{N}\sum_{j\neq i}^{N} \delta\left(r - r^{ij}\right)\right\rangle, \qquad (12)$$

where ρ is the number density $\frac{N}{V}$. With increasing degree of crosslinking, each bead is connected to more number of beads through harmonic interactions, which leads to crowding of the beads in the nearest neighbor coordination shell around a given bead. In Figure 2, $g(r)$ is plotted against the scaled bead-to-bead distance, with the relative height of the first peak indicating how crowding is impacted by the degree of crosslinking. Since the

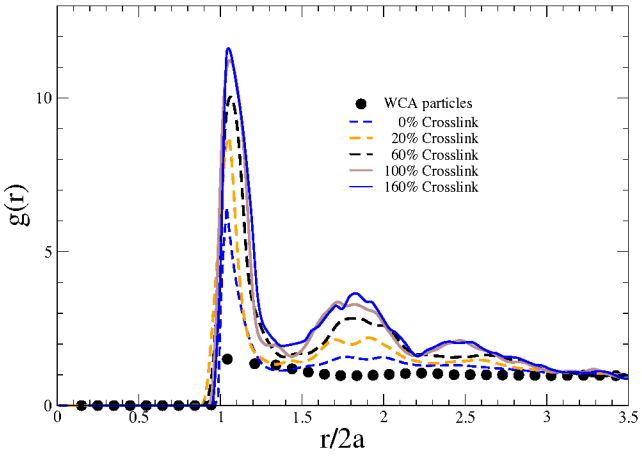

Fig. 2 Radial distribution functions of bead positions in NCs with different crosslinking densities. For comparison, the $g(r)$ for an equivalent system of free WCA particles (i.e., not constrained by any Kuhn or crosslinking interactions) is also depicted.

beads in NC are in close proximity, crowding of beads also likely impacts the movement of each test bead. Hence, we use a Voronoi diagram analysis in order to allocate a fluid volume element to each bead, and we calculate the neighbor statistics and the volume of the Voronoi elements for each bead. We follow Rycroft [37] to generate a Voronoi volume around each bead (Figure 3(a)). However, since the beads are clustered in a network, leading to an inhomogeneity in the structure, an irregular Voronoi tessellation is more appropriate for such structures, as depicted in Figure 3(b).

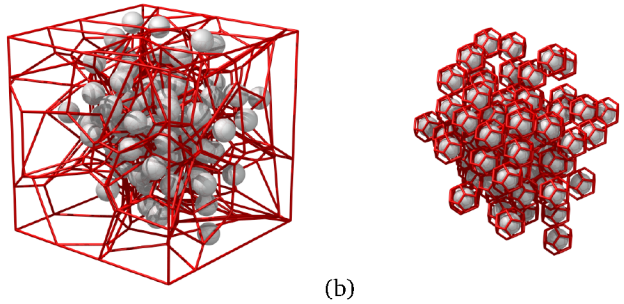

Fig. 3 (a) Periodic Voronoi tessellation around the beads, (b) Irregular Voronoi tessellation around the beads of the NC; here the gray spheres represent the beads and the red lines represent the skeleton of the Voronoi tessellated lattice.

A star polymer without any crosslinking shows arm retractions, which can be captured by collecting the volume of each Voronoi cell and then plotting the probability density function of

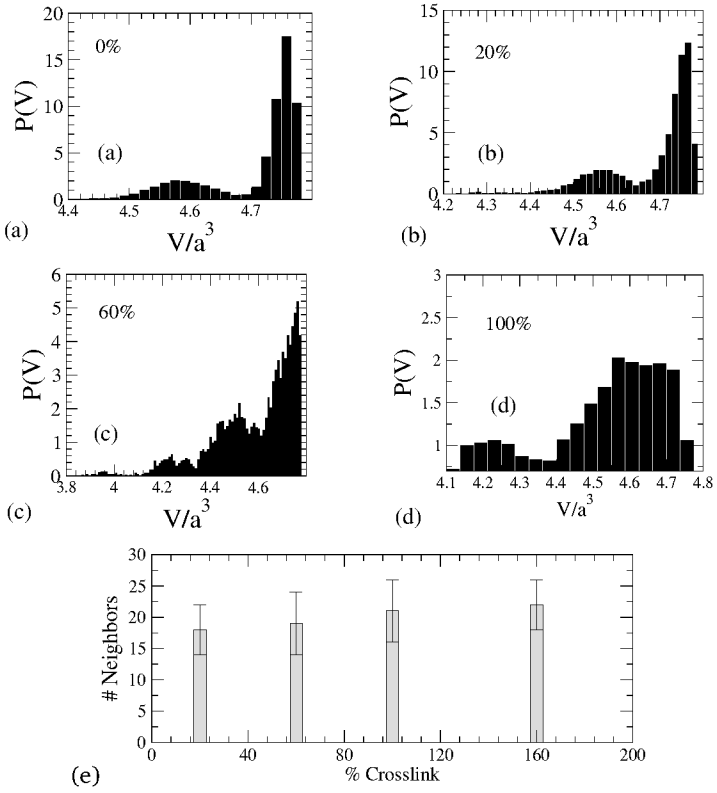

Fig. 4 (a)-(d) Distributions of Voronoi tessellated cell volumes ($P(v)$) for different crosslinking densities, (e) Number of nearest neighbors for different crosslinking.

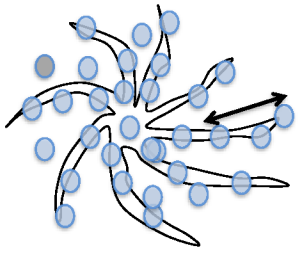

Fig. 5 Schematic of a star polymer configuration. The two headed arrow shows the direction of arm retractions.

the Voronoi-cell volumes of the beads. In Figure 4 the probability distributions of Voronoi-cell volumes for different crosslinked densities are shown. The characteristic bimodal distribution is a reflection of the star-shaped conformation of the NC, where there is a clear separation of the Voronoi-cell volumes associated with the outer radial (arm) regions, and those in the inner-regions of the NC including the core, see Figure 5. With increasing crosslinking, the distribution of volumes shift and the demarkation of the two afore-mentioned regions becomes increasingly nebulous with increasing crosslinking.

With increasing crosslinking the distribution of nearest neighbors is also altered. Specifically, to estimate the number of nearest neighbors, we calculate the area around a bead and divide by the projected area between a pair of beads, (which for spherical beads would yield a value of π in scaled units). The average number of nearest neighbors (over a period of $75\frac{a^2}{D_o}$ is estimated to be between 16–20) and is plotted against % crosslinking in Figure 4(e), which clearly shows that with increase in crosslinking, there is a corresponding increase in the crowding of beads.

4.2 Radius of Gyration and Diffusivity

In order to characterize the size of the NC, we compute the radius of gyration (R_g) based on bead positions. For a model with all the beads being the same mass, the radius of gyration tensor ($\boldsymbol{G}$) is defined as

$$\boldsymbol{G} = \frac{1}{N}\sum_{i=1}^{N}\left(\boldsymbol{r}^i - \boldsymbol{r}^{cm}\right)\left(\boldsymbol{r}^i - \boldsymbol{r}^{cm}\right), \tag{13}$$

where cm denotes center of mass of the NC beads. The characteristic size along three orthogonal directions is denoted by the eigenvalues λ_i $(i = 1,3)$ of the matrix $\mathbf{G}$, and the radius of gyration is defined as :

$$R_g^2 = \sum_{m=1}^{3}\lambda_m. \tag{14}$$

In Figure 6(a), the radius of gyration is plotted against the crosslinking density, showing that with increasing crosslinking, the radius of gyration decreases.

Since, the NC size is shown to decrease with increasing crosslinking, we hypothesized that the crosslinking will also influence the self diffusivity of NC. To test this hypothesis, we compute mean squared displacement (MSD) and compute the self-diffusivity (D_s) of the NC. MSD is defined as:

$$\left\langle\left[\boldsymbol{r}^i(t_o+t) - \boldsymbol{r}^i(t_o)\right]^2\right\rangle = 6D_s t, \tag{15}$$

where $\boldsymbol{r}^i$ represents the absolute position of bead i, D_s is self-diffusivity of the NC and t is the trajectory time. Here, the ensemble average is taken over all the beads.

For 160% crosslinked NC, the radius of gyration $R_g/a \approx 4.3 \pm 0.3$ and the self-diffusivity is calculated to be $D_s/D_o \approx 0.15$. It is already evident from the $g(r)$ data (Figure 2) that the 160% crosslinked microstructures represent the highest degree of closed packing in terms of conformations. We, therefore, compare the diffusivity of the 160% crosslinked nanocarrier with theoretical prediction for hard spheres: we compute the volume fraction

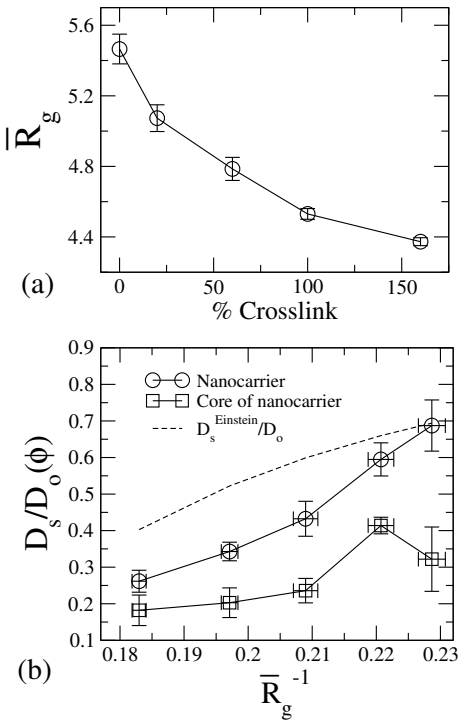

Fig. 6 (a) Radius of gyration of NC for various crosslinking densities; the radius of gyration is nondimensionalized with the radius of the beads. (b) Diffusivity of the beads and of the core of the NC against the radius of gyration, R_g.

based on radius of gyration of 160% crosslinked nanocarrier and compute corresponding diffusivity based on Einstein's correction to intrinsic viscosity of hard spheres, i.e., $D_s^{\text{Einstein}}(\phi) = \frac{D_s(\phi=0)}{1+2.5\phi}$. The calculated diffusivity of the NC based on MSD is i.e. $\frac{D_s}{D_o}(\phi) = 0.68$. This computed value is in close agreement with the estimate based on the Einstein correction; for a hard sphere of radius $4.3a$, $\phi = 0.15$ and $\frac{D_s^{\text{Einstein}}}{D_o} = 0.71$, suggesting that the 160% crosslinked NC shows diffusion very similar to that of hard spheres. We plot $\frac{D_s}{D_o}(\phi)$ against R_g for the NC and for the NC-core in Figure 6(b). The diffusivity varies inversely with the radius of gyration for the NC as well as for the NC-core. It is clear from Figure 6(b) that the core of the NC microstructure also exhibits Brownian motion. Since, the environment surrounding the core has the highest density of beads, the diffusivity of the NC-core is reduced relative to that of the NC. However, since the core follows the center of mass of the NC, the self-diffusivity of the core tracks that of the center of mass of the NC microstructure, and with increasing diffusivity of NC, the self-diffusivity of the core also increases (see Figure 6(b)).

The characteristic size of the NC can be estimated from the root-mean-squared end-center distance, which is a closely related quantity to the radius of gyration. If there are f number of arms, with N_b number of beads in each arm, then the mean-squared end-center distance is defined as:

$$\left\langle R_{\text{arm}}^2 \right\rangle = \left\langle \frac{1}{f} \sum_{k=1}^{f} \left[\boldsymbol{r}^{\text{core}} - \boldsymbol{r}^{k,N_b} \right]^2 \right\rangle, \tag{16}$$

where $\boldsymbol{r}^{core}$ is position of core and $\boldsymbol{r}^{k,N_b}$ is the position of the last bead in the k^{th} arm. We compute the end-to-center distance (R_{arm}) of the NC using equation (16). Significantly, the simulated end-to-center distance of the polymer is estimated to be $144-184$nm (for crosslinking density in the range $20-160\%$), which compares very favorably to the measured size of $120-180$nm for the NC[16]. This favorable comparison justifies our choice of utilizing 25-arms per NC in our coarse-grained model.

4.3 Structure factor

To complete our analysis of the NC structure, we compute the structure factor, defined as:

$$S(\boldsymbol{k}) = \left\langle \frac{1}{N} \left| \sum_{j=1}^{N} \exp\left(-i\boldsymbol{k}\cdot\boldsymbol{r}^j\right) \right|^2 \right\rangle, \tag{17}$$

where $\boldsymbol{k}$ is the wave vector, $\boldsymbol{r}^j$ represents the position of bead j, and the average represents an average over the trajectory. In Figure 7, we choose $\boldsymbol{k} = (k,0,0)$ and plot $S(k)$ against k. The large k behavior characterizes the NC internal structure (form factor), while the small k behavior characterizes the overall NC packing. In particular, we argue that $S(k = \frac{2\pi}{R_g})$ will track the overall compressibility of the NC. This value of k can also be regarded as differentiating between the large k behavior and the small k one. We note that the justification for scaling k with R_g (instead of with a) is based on the model proposed by Grest *et al.* [18] and by Prentis [19], where equation (17) is approximated in the limit $kR_g \ll 1$ as:

$$S(k) \approx N\left(1 - \frac{1}{3}k^2\left\langle R_g^2\right\rangle + \ldots\right). \tag{18}$$

Hence, when we rescale k with $\frac{2\pi}{R_g}$ and plot $\frac{S(\bar{k})}{S(0)}$ in Figure 7, we find that the data collapse into a single master curve for $kR_g \ll 1$ (specifically for $\bar{k} \ll \frac{\sqrt{3}}{2\pi}$). The terrace-like behavior for $\bar{k} \ll 1$ is also consistent with the trends reported in other computational studies of star polymers of large molecular weight, and in neutron scattering of microgels[38]. The differences in the curves for $\bar{k} > 1$ reflects the differences in internal structure of the NC (or in form factors) caused by changing the crosslinking densities.

Since, with increasing crosslinking, the radius of gyration decreases (see Figure 6(a)), we surmise that the normal stress or pressure (P) should scale as $\frac{P}{k_BT} \sim R_g^{-d}$, (i.e. increase with increasing crosslinking). We show in Figure 7 (inset) that $S\left(\frac{2\pi}{R_g}\right)$ decreases with increasing crosslinking, which indicates an increase in compressibility as a consequence of increased pressure. In this discussion, the scaling exponent d can simply represent the dimensionality for dilute systems, or can be significantly different from dimensionality for strongly correlated systems; we explore this scaling of pressure with R_g in a latter section dealing with the direct calculation of stresses.

The static properties discussed here will also be impacted by the deformation of the NC under shear flow, which is discussed in Section 5.

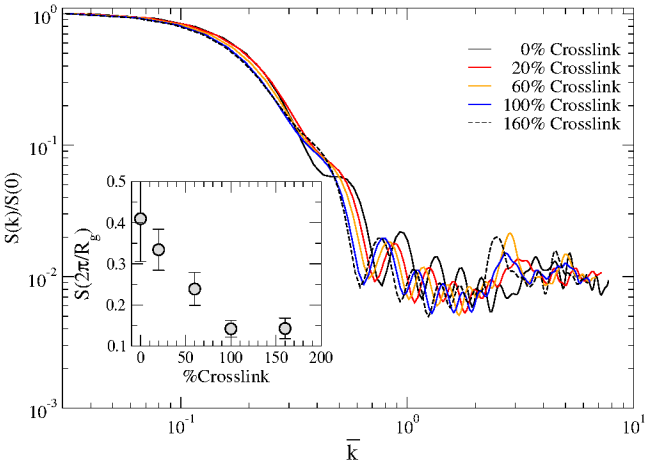

Fig. 7 Static structure factor $S(k)$ and $S(\frac{2\pi}{R_g})$ (inset) at various crosslinking densities. The wave vectors are scaled with $\frac{2\pi}{R_g}$ i.e. $\bar{k} = \frac{kR_g}{2\pi}$.

5 Dynamic Properties: Results and Discussion

The dynamic properties are studied to investigate the response of the NC to shear forces. The context we consider is that of blood capillaries of radius typically 5 times the radius of red blood cells (RBCs). The characteristic radius of a RBC is $a_{RBC} = 2.5\mu m$. Under flow, the RBCs in a capillary migrate to the center, therefore, causing the NCs to marginate to the cell free layer[3]. The cell-free layer represents the gap between the RBC-occupied core and the wall of the capillary, which is $2a_{RBC}$ (see Figure 8). We consider a physiologically relevant shear near the endothelium (shown in Figure 8). Yeh and Eckstein[39] have measured wall shear in blood flow in the range of $785–1250s^{-1}$. Considering viscosity of blood plasma as 1.3mPa.s, and based on our bead radius a, we calculate the maximum Péclet number $Pe = \frac{\dot{\gamma}_\infty a}{D}$ to be 5. However, we explore the range of $0 \leqslant Pe \leqslant 5$, where the lower end, the range corresponds to flow rate in smaller capillaries as well as lymphatic flows[3,40].

In our simulations, a steady shear is applied along the $r_1 - r_2$ direction, where r_1 is the shear direction and r_2 is the gradient direction, see Figure 9(b). We solve equation (11) for bead positions with the Lees-Edward boundary condition[41] for a given shear rate. We mostly represent our results interms of the Weissenberg number (Wi), defined as $Wi = \dot{\gamma}\tau_a$, where $\dot{\gamma}$ is the shear rate, and τ_a is the relaxation time of the NC, i.e., $\tau_a = \frac{R_g^2}{D_g}$. Since Pe is defined interms of the radius of the beads, for linear polymers $\frac{Wi}{Pe} \sim \frac{R_g^3}{a^3}$. Grest *et al.*[42] investigated the relaxation of self-entangled star polymers and showed that the star polymers relax faster than their linear counter-parts, and that the ratio of the relaxation times scales as $f^{-\frac{1}{2}}$. Hence, for the present case, $\frac{Wi}{Pe} = f^{-\frac{1}{2}}\frac{R_g^3}{a^3}$.

Under shear (see Figure 9(a)), the NC undergoes stretching and the crosslinked bonds resist deformation (see Figure 9(b)). Depending on the crosslinking density and the shear rate, the NC orients at an angle θ with the shear direction (see Figure 9(c)). While, the angle θ contains critical information about the strain

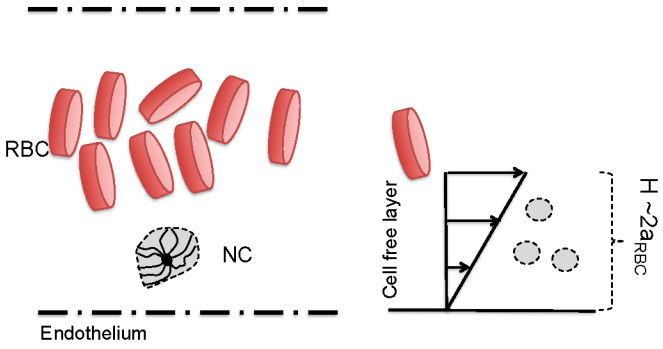

Fig. 8 Schematic of a marginated NC in a blood capillary near the endothelium.

response of the NC, due to crosslinking the deformation of the NC along r_3 (orthogonal to the shear plane) would also depend on the shear rate (see Figure 9(d)). Internal stresses originate from bead-to-bead interactions and stretching of the bonds. In particular, the configurational stresses arise from bond stretching, while forces due to deformation can lead to an increase in the collisional stresses.

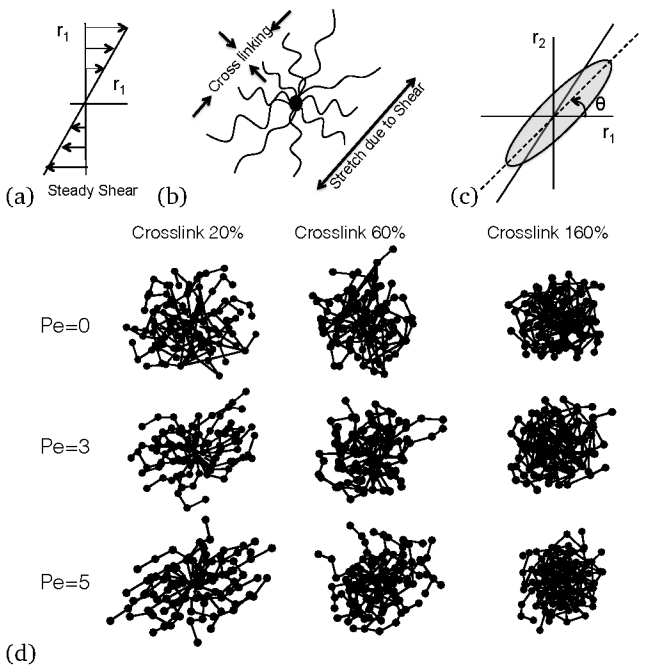

Fig. 9 (a) Direction of the applied shear; (b) schematic of a sheared NC, (c) angle of inclination of the sheared NC; (d) simulation results of representative bead positions showing connected bonds. With increasing shear rate, an ellipsoid or a rod-like conformation is observed, which inclines more towards the shear direction at an angle θ to shear direction. With increasing crosslinking, the nanocarrier changes the inclination angle as well as the shape.

In addition to the internal stresses, the tumbling of the NC can cause an additional mode of relaxation to an already complex phenomenon. Hence, below, we explore the effect the shear and crosslinking on NC shape, deformability, tumbling behavior, shear and normal stress distributions.

5.1 Shape of NC under shear

Deformation of the NC is computed from the components of radius of gyration tensor (**G**). Eigen values of the radius of gyration tensor defined in equation (13) are used to calculate degree of prolateness, defined as,

$$S = \frac{27\left\langle \prod_i^3 (\lambda_i - \bar{\lambda}) \right\rangle}{\left\langle \left(\sum_i^3 \lambda_i \right)^3 \right\rangle}, \qquad (19)$$

where $\bar{\lambda} = \frac{1}{3}\left(\sum_i^3 \lambda_i\right)$. In prior studies S has been shown to vary from -0.25 to 2, where the change in sign from '-ve' to '+ve' signifies an oblate to a prolate shape change[43]. In Figure 10, S is plotted against the shear rate, and as evident, with increasing shear rate the NC undergoes deformation and assumes a shape that is similar to a prolate spheroid. In particular, the NC without crosslinking undergoes a large deformation (see inset of Figure 10), and with increasing crosslinking densities, the degree of prolateness is smaller, Figure 10.

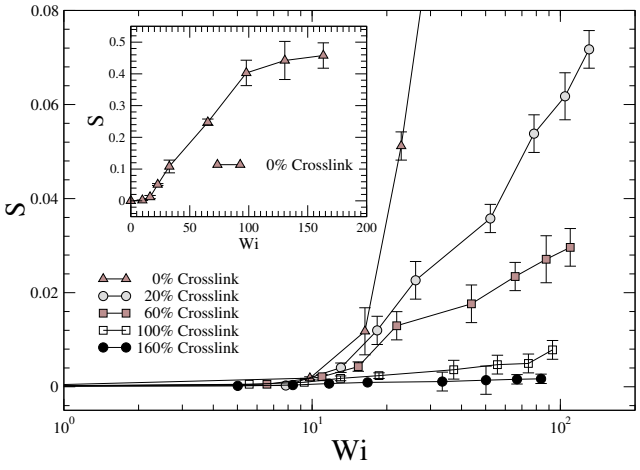

Fig. 10 Prolateness of NC versus shear (Pe) and crosslinking density.

Ripoll et. al.[20] have investigated the effect of shear on the asphericity of a star polymer, which is a measure analogous to S. To quantify the extent of deformation due to shear, the asphericity is computed as $\frac{\lambda_1}{\lambda_3} - 1$, where $\lambda_1 \geqslant \lambda_2 \geqslant \lambda_3$, see Figure 11; we note that $\frac{\lambda_1}{\lambda_3} - 1 = 0$ corresponds to a sphere. We find that for NC with 0% crosslink which is closest to the star polymer approximation, our results are in close agreement with those of Ripoll et. al.[20] as shown in Figure 11.

With increasing crosslinking the resistance to deformation increases and hence our results deviate from the 0% crosslink density case. In particular, the deformation is low and shows a much weaker dependence on Pe. However, as discussed later, the deformation along the gradient direction offers information on the effect of shear on the stiffness of of the NC.

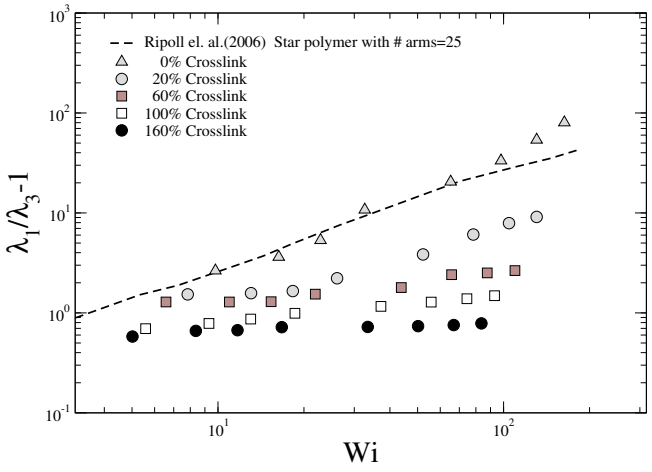

Fig. 11 Degree of deformation of NC for various shear rates and crosslinking densities, quantified in term of the asphericity.

5.2 Internal structure of NC under shear

We now consider how the spatial distribution of beads is perturbed in the shear flow field. Unlike the zero shear case considered in Section 4, we consider the radial distribution function as a perturbation expansion along the plane of shear, and compute the 1st perturbation to the radial distribution function shown in equation (20). Strating[44] has showed that

$$g(r) \quad = \quad g_o(r) + 2Pe\frac{r_1 r_2}{r^2} g_1(r) + O(Pe^2). \qquad (20)$$

Here, $g_o(r)$ is equilibrium radial distribution function, $g_1(r)$ is 1st perturbation to radial distribution function $g(r)$. The orientation in the stretch direction is represented by θ, and ϕ represents the azimuthal angle. In Figure 12, we plot $g_1(r)$, which we calculate using the relationship:

$$g_1(r) = \frac{1}{N\rho}\left\langle \sum_i^N \sum_{j\neq i}^N \delta\left(r - r^{ij}\right) \sin^2\theta \sin\phi\cos\phi \right\rangle. \qquad (21)$$

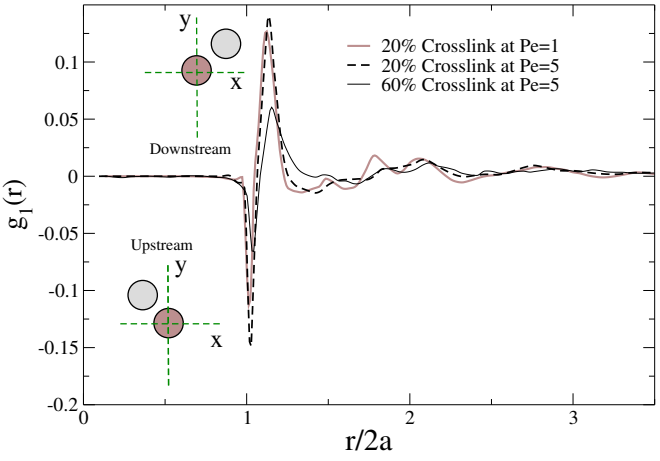

Fig. 12 1st perturbation to radial distribution function in shear flow field for different crosslinking and Péclet number.

In a shear field, two beads approach each other in the upstream configuration and rotate to a downstream configuration. In the upstream configuration, the $g_1(r)$ is negative while in the downstream configuration it is positive; however, the spring restoring force acts against shear, and since the beads are connected, a given pair of beads that rotates from upstream to downstream also show spring and tumbling relaxations that depend on *Pe* and the degree of crosslinking of NC. Hence, the internal structure of the NC gets perturbed by the shear, and the degree of perturbation is strongly dependent on *Pe* and % crosslinking.

Due to the prolate shape of the NC (see Figure 10), the majority of the bead-to-bead contacts originates from the orientation orthogonal to the shear direction, chiefly contributed by the deformation. Since, the difference in the area under the $g_1(r)$ curve is anti-symmetrical (i.e. the depletion upstream is matched by the enhancement downstream), the collisional stresses contribute less to the overall shear stress. Hence, for a given crosslinking density, there is no significant change in the $g_1(r)$ function with *Pe*. For a similar shear rate, however, with increasing crosslinking, there is a significant shift in the $g_1(r)$ curve, suggesting that the increased crosslinks cause the NC to resist shear deformation, and perhaps contribute significantly to the build-up of internal stress. In Subsection 5.4, stresses computed independently from the Virial expression, also support the observations gleaned from the 1st perturbation to the radial distribution function.

5.3 Comparison of NC deformation under shear with related models of polymer assemblies

The stresses induced are caused by the stretching of bonds which results in deformation of the microstructure and the corresponding strain is computed from components of radius of gyration tensor (**G**). The configuration thickness (δ_2) is defined as

$$\delta_2 = \sqrt{G_{22}}, \quad \text{and} \quad \bar{\delta}_2 = \frac{\delta_2}{\delta_2(Pe=0)}. \tag{22}$$

The ratio of shear and normal strain difference determines the orientation[45] of the NC, given by:

$$\tan(2\theta) = \frac{2G_{12}}{G_{11} - G_{22}}, \tag{23}$$

where θ is configurational orientation of the NC. The configurational thickness and configurational orientation calculated from equation (22) and equation (23) are plotted in Figure 13, where $\langle\theta\rangle$ and $\langle\bar{\delta}_2\rangle$ for various shear rates and crosslinking densities are depicted. Since the applied shear is in the r_1 direction, with r_2 being the gradient direction, G_{12} represents the shear strain, and $G_{11} - G_{22}$ represents the 1st normal strain difference. We plot the configuration thickness as well as the NC orientation against time in Figure 14(a), which together indicate how the configuration thickness associated with change in shape of the NC is related to the NC tumbling motion. The correlated motion in θ versus t and δ versus t clearly suggests that the tumbling motion is a mechanism by which the system relieves the build-up of internal stress. It is also intriguing to note that the tumbling relaxation time is highly sensitive and decreases with increasing degree of crosslinking.

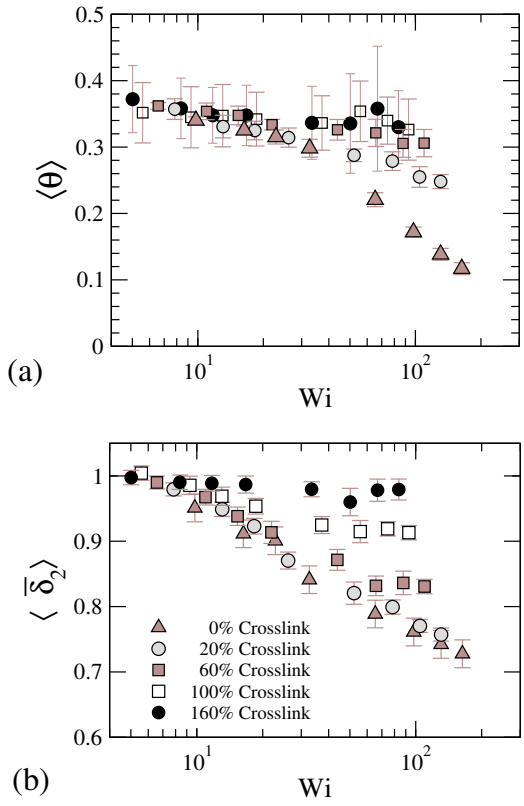

Fig. 13 (a) Configurational orientation and (b) configurational thickness for various *Wi* and crosslinking densities.

In a linear response model, the ratio of the applied force to the deformation represents a "stiffness": for e.g., in the case of a Hookean spring, the stiffness constant $K_{\text{spring}} = |\text{force}|/|\text{displacement}|$. Since, δ_2 depends on *Wi*, Teixeira *et al.*[45] have introduced a general relationship: $\delta_2 \sim Wi^{-n}$ in order to compare various models. Since *Wi* can be regarded as an applied force and $1/\delta_2$ as an effective deformation, the stiffness or resistance to configurational thickness can be measured by the product $\langle\delta_2\rangle Wi$. Figure 14(b) shows the averaged configurational thickness resistance ($\langle\delta_2\rangle Wi$). Fits to the data indicate the configurational thickness resistance increase with increasing crosslinking. That is, the configuration thickness scales as $Wi^{-0.01}$ for 0% crosslinking and as $Wi^{-0.11}$ for 160% crosslinking. Teixeira *et al.*[45] have previously shown that for a linear worm-like chain (WLC) polymer system $\langle\delta_2\rangle \sim Wi^{-0.26}$. Here, compared to the Teixeira *et al.*[45] result for a soft linear system, $\langle\delta_2\rangle$ is relatively weak function of *Wi* for all NC.

Due to the prolate shape of the NC under shear, the stresses are not only dependent on the deformation but also on the orientation of the nanocarrier, which is evident from Figure 13 and Figure 14. In particular Figure 10 and Figure 11 show that under shear, a large degree of crosslinking leads to sphere-like shapes, while smaller degree of crosslinking leads to NC shapes approaching rod-like geometries. Moreover with the deformation field along the $r_1 - r_2$ direction, and increasing shear, the NC tumbles (Figure 14(a)) and the average orientation over the tum-

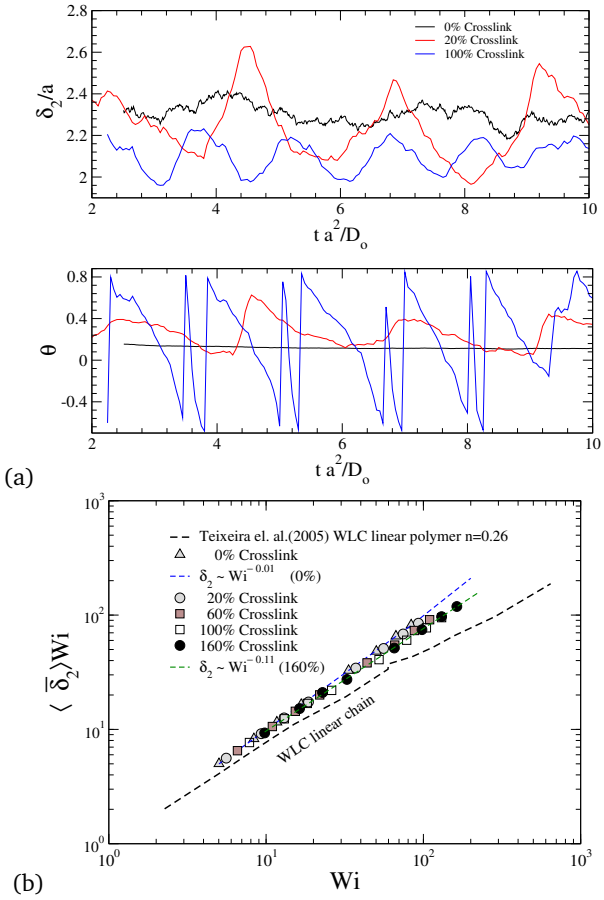

Fig. 14 (a) Time evolution of configurational thickness and NC orientation for various crosslinking densities at $Pe = 5$. (b) Configurational thickness resistance for various Wi and crosslinking densities.

bling cycle gives important information regarding ratio of shear strain to normal strain difference, see equation (23). The rheological response of rod-like particles, under small shear, is described by $G_{12} \sim Pe$ and $(G_{11} - G_{22}) \sim Pe^2$ [46,47], for which $\tan(2\theta) \sim \frac{1}{Pe}$. Since $Wi \sim Pe$, the scaling for rod-like particles corresponds to $\tan(2\theta) \sim Wi^{-1}$, as indicated in Figure 15.

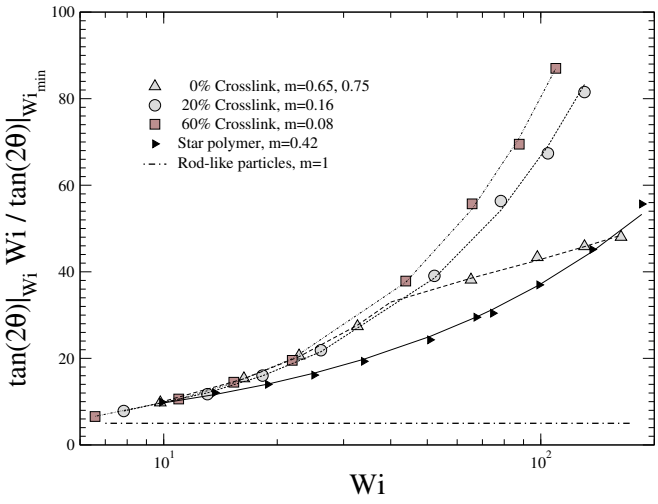

Fig. 15 $\frac{\tan(2\theta)|_{Wi} Wi}{\tan(2\theta)|_{Wi_{min}}}$ for various Wi and crosslinking densities.

In contrast, a star polymer's orientation can be expressed as function of the Wi and it has been shown that $\tan(2\theta) \sim Wi^{-m}$, where $m \sim 0.35 - 1$ [20,21,45]. In Figure 15 we plot $\frac{\tan(2\theta)}{Wi}$ for various shear rates and crosslinking densities, and show the corresponding fits to the data by reporting the values of m; we omit results for large crosslinking densities (100% and 160%) due to their spherical shape (see Figure 13). It is evident that the behavior of NC with smaller degrees of crosslinking approach the scaling for rod-like particles.

For ultra soft colloids investigated by Singh *et al.* [21] $m = 0.43$, by Ripoll et.al. [20] $m = 0.35$, while Teixeira *et al.* [45] have shown that for long linear WLC polymers, $m = 0.46$. Our results in Figure 15 indicate that m decreases with decreasing crosslinking; stated differently, m decreases as the degree of deformation (shown as $\frac{\lambda_1}{\lambda_3} - 1$ in Figure 11) of the NC increases.

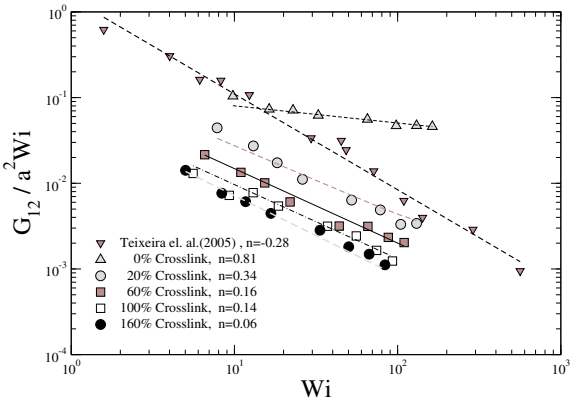

Fig. 16 $\frac{G_{12}}{a^2 Wi}$ for various Wi and crosslinking densities. The data are fit to a power law curve: $G_{12} \sim Wi^n$.

In Figure 16, the ratio of shear strain G_{12} to Wi is plotted for various shear rates and crosslinking densities. A decrease in $\frac{G_{12}}{Wi}$ indicates a decrease in the first normal strain coefficient which is akin to the effective viscosity of a single NC[45], which is observed for increasing crosslinking. In particular, the exponent governing the decrease in the first normal strain coefficient with Wi of the crosslinked NC is similar to that reported in single molecule experimental results shown by Teixeira *et al.* [45]. The 0% crosslinked NC at large shear rate, is highly stretched and approaches $G_{12} \sim Wi$, which is close to that for a rod-like polymer response to steady shear flow.

5.4 Internal stresses and stiffness of the NC under shear

We calculate internal stresses to estimate the response of NC to the observed structural changes. Following Irving and Kirkwood[48], (see Appendix A for derivation) stresses are calculated using the expression:

$$\bar{\boldsymbol{\sigma}} = -\left\langle \sum_{ij} \bar{\boldsymbol{r}}_{ij} \bar{\boldsymbol{F}}_{ij} \right\rangle \tag{24}$$

where $\boldsymbol{\sigma}$ is the stress tensor, $\boldsymbol{F}_{ij}$ is force on bead i due to bead j, and $\boldsymbol{r}_{ij}$ is the distance vector between the beads i and j.

In Figure 17(a) the shear stresses $(\frac{\bar{\sigma}_{12}}{Pe} \frac{Pe^*}{\bar{\sigma}^*_{12}})$ is plotted for various shear rates, confirming that the NC under shear, shows shear thinning akin to Figure 16, and the shear thinning effect is significantly higher than that reported for hard spheres suspensions[49].

We have shown that with increasing crosslinking the radius of gyration of the NC decreases (Figure 6) and the stiffness of the NC increases (Figure 7), causing us to hypothesize that there is a likely build-up of normal stress. To directly test this hypothesis, we compute the trace of the stress tensor, i.e., $\frac{P}{\rho k_B T} = \sum_{i=1}^{3} \bar{\sigma}_{ii}$. In Figure 17(b), the computed normal stress $(\frac{P}{\rho k_B T})$ is plotted for various shear rates and for different crosslinking. For smaller crosslinking the normal stress increases with shear, and the shear dependence gets weaker with increasing crosslinking density; for the largest crosslinking we consider the normal stress is independent of shear. This trend is also consistent with those discussed in Figure 11, which shows that the deformation of a highly crosslinked NC is a weak function of shear. Our data in Figure 17(c) validates our hypothesis that the stiffness of the NC originates from the osmotic pressure by clearly showing that with decreasing radius of gyration, the normal stress increases. For dilute suspensions, the osmotic pressure $\sim R_g^{-3}$, however as shown in the figure, the exponent of -8.28 indicates that the intrinsic stress build-up is significantly larger than that expected from a dilute system. Below, we explore the mechanism contributing to the intrinsic stress through a simple theoretical model from the literature.

In their textbook, Dill and Bromberg[50] have described a network of freely jointed chains to explain the elasticity of networked polymers and have expressed the free energy (F) as a function of strain subject to a volume conservation constraint, given by:

$$\Delta F = E\left(L_1^2 + L_2^2 + L_3^2 - 3L_o^2\right) \tag{25}$$

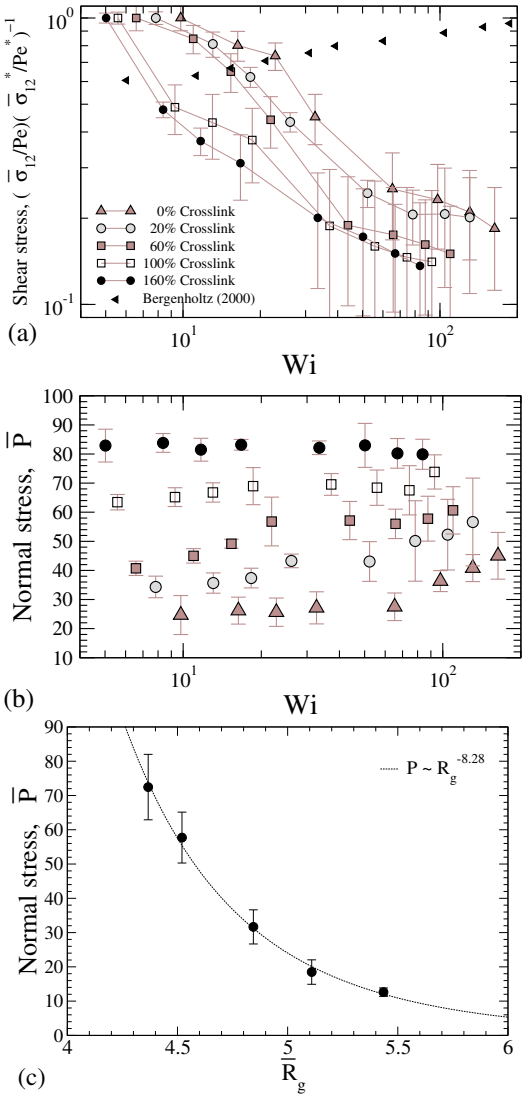

Fig. 17 (a) Shear stress $\frac{\bar{\sigma}_{12}}{Pe} / \frac{\bar{\sigma}^*_{12}}{Pe^*}$); (b) normal stress at different crosslink densities; (c) normal stress plotted versus the radius of gyration.

where, the elongation ratio $\bar{L} = \frac{L}{L_o}$ (where $L_o = L_{Wi=0}$) and $\frac{E}{L_o}$ is a modulus of elasticity. We approximate the volume of the NC at $Wi = 0$ as a sphere of diameter L_o (i.e.$L_{io} = L_o$). For $Wi > 0$, the normal stress difference (based on the direction of stretching) deforms the NC from a sphere to an ellipsoid. From the volume conservation condition we get:

$$\frac{4\pi}{24} L_1 L_2 L_3 = \frac{4\pi}{24} L_o^3$$

$$\therefore \quad L_1 L_2 L_3 = L_o^3. \tag{26}$$

The normal stress difference defined as:

$$\sigma'_N = \sigma'_1 - \frac{1}{2}(\sigma'_2 + \sigma'_3) \tag{27}$$

where σ'_1 is the stress along the direction of stretch and σ'_2 and σ'_3 are stresses orthognal to σ'_1. We assume that the deformation of NC is symmetric along the directions orthogonal to stretching direction i.e. $L_1 = L$ and $L_2 = L_3$. We obtain from equation (25) and equation (26):

$$\Delta F = E\left(L^2 + \frac{2L_o^3}{L} - 3L_o^2\right)$$

$$\therefore \quad \sigma'_N = \frac{d\Delta F}{dL} = \frac{2E}{L_2 L_3}\left(L - \frac{L_o^3}{L^2}\right) = \frac{2EL}{L_o^3}\left(L - \frac{L_o^3}{L^2}\right)$$

$$\therefore \quad \sigma'_N = \frac{2E}{L_o}\left(\bar{L}^2 - \frac{1}{\bar{L}}\right). \tag{28}$$

In the above-described model, it can also be stipulated that the network consists of m freely jointed chains each with N_k links of length b_k, and one can relate the force (f_1) needed for a given elongation L_1, from which the force per unit area can be written as:

$$\frac{f_1}{L_2 L_3} = \frac{3mk_BT}{Nb^2 L_2 L_3}\left(L - \frac{V_o}{L^2}\right)$$

$$\therefore \quad \sigma'_N = \frac{3mk_BT}{N_k {b_k}^2 L_o}\left(\bar{L}^2 - \frac{1}{\bar{L}}\right). \tag{29}$$

Comparing equation (28) and equation (29), $E = \frac{3mk_BT}{2N_k {b_k}^2}$. For small elongation we assume that $\bar{L} = 1 + \varepsilon$ and we get:

$$\sigma'_N = \frac{6E}{L_o}\varepsilon. \tag{30}$$

If C is the modulus of elasticity of the NC, then $C = \frac{6E}{L_o}$. We calculate the eigenvalues of radius of gyration tensor equation (13). We define the elongation L as $\sqrt{\frac{\lambda_1}{\lambda_{1\,Wi=0}}}$ where λ_1 is the eigenvalue of the radius of gyration tensor along the direction of elongation. Similarly, we calculate the eigenvalues of the stress tensor equation (24) and the normal stress difference is calculated from equation (27). In Figure 18 the normal stress difference $\bar{\sigma}'_N$ is plotted against elongation $\bar{L}$.

We fit the data for the normal stress difference for each crosslinking density (dotted lines in Figure 18) for small elongations as shown in equation (28), from which we further estimate the elasticity modulus (C). We find that with increasing crosslinking the elasticity modulus increases from 0.4 to 15 kPa.

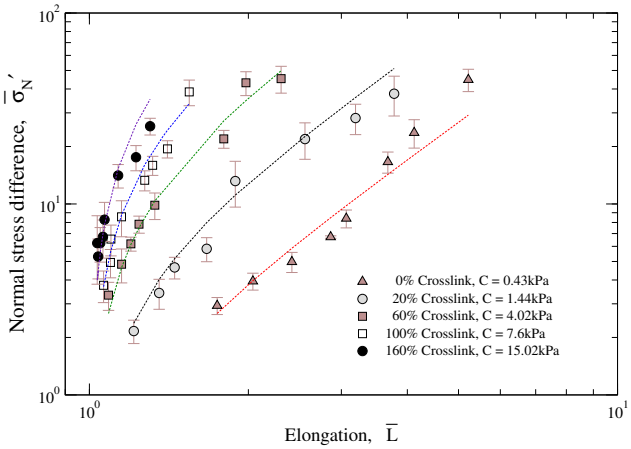

Fig. 18 Normal stress difference versus elongation for various crosslinking densities.

Table 1 Computed stiffness of the NC and the measured structural stiffness of common biomaterials.

Material type	Method	Stiffness	Ref.
Confluent endothelial monolayers	experimental	0.1 – 0.8Pa	Dewey *et al.* [51]
Chondrocytes	experimental	0.5kPa	Hochmuth [52]
Human platelets	experimental	1.5 – 4kPa	Mathur *et al.* [53]
Endothelial cells	experimental	1.4 – 6.8kPa	Mathur *et al.* [53]
Nanocarrier	calculated	0.4 – 15 kPa	
Skeletal muscle cells	experimental	24.7 ± 3.5kPa	Mathur *et al.* [53]
Cardiac cells	experimental	100.3 ± 10.7kPa	Mathur *et al.* [53]

We also compare the calculated stiffness of the NC with previously measured stiffness of soft and hard biomaterials in Table 1, and we find that the stiffness of the NC falls in the range of moderately soft materials.

6 Conclusion

We have developed a model for a new class of highly deformable polymer based NC synthesized by Coll Ferrer *et al.* [11,16] and Ferrer *et al.* [15]. We explored zero shear properties of the microstructures as well as demonstrated the effects of physiologically relevant shear on the structure and dynamic properties of the NC. Our findings are also consistent with other theoretical findings in limiting cases. We believe that the development of such models is essential to gain useful insights that can be translated into the optimal design of nanocarriers for targeted drug delivery. Future work will focus on combining this model with previous models for functionalized NCs [54,55] to include adhesive interactions, along with experimental investigation in-vitro and in-vivo. Together, these will advance our understanding of the binding affinities of soft crosslinked NCs to cells.

We acknowledge support from NIH through grants NIH 1R01EB006818-05.

A Intrinsic Stress

Following Irving and Kirkwood [48], the stress tensor is given by:

$$\boldsymbol{\sigma}(\boldsymbol{r},\boldsymbol{t}) = -\frac{1}{V}\left[\sum_i m_i(\dot{\boldsymbol{r}}_i - \boldsymbol{v}_\infty) + \frac{1}{2}\sum_{ij}\boldsymbol{r}_{ij}O_{ij}\boldsymbol{F}_{ij}\,|_{\boldsymbol{r}_i=\boldsymbol{r}}\right], \quad (31)$$

where, O_{ij} is the differential operator given by:

$$O_{ij} = 1 - \frac{1}{2!}\boldsymbol{r}_{ij}.\frac{\partial}{\partial \boldsymbol{r}} + \cdots + \frac{1}{n!}\left[-\boldsymbol{r}_{ij}.\frac{\partial}{\partial \boldsymbol{r}}\right]^{n-1} + \cdots \quad (32)$$

We scale stresses by nk_BT, where n is the number density of beads, k_B is the Boltzmann constant, and T is the temperature, and rewrite the expression for stresses as:

$$\begin{aligned}\bar{\boldsymbol{\sigma}}(\boldsymbol{r},\boldsymbol{t}) &= -\frac{1}{N}\left[\sum_i \frac{m_i D_o}{k_B T a}(\dot{\bar{\boldsymbol{r}}}_i - \bar{\boldsymbol{v}}_\infty) + \frac{1}{2}\sum_{ij}\bar{\boldsymbol{r}}_{ij}\bar{O}_{ij}\bar{\boldsymbol{F}}_{ij}\,|_{\boldsymbol{r}_i=\boldsymbol{r}}\right]\\ &= -\frac{1}{N}\left[\sum_i \frac{\tau_I}{\tau_D}(\dot{\bar{\boldsymbol{r}}}_i - \bar{\boldsymbol{v}}_\infty) + \frac{1}{2}\sum_{ij}\bar{\boldsymbol{r}}_{ij}\bar{O}_{ij}\bar{\boldsymbol{F}}_{ij}\,|_{\boldsymbol{r}_i=\boldsymbol{r}}\right]\\ &= -\frac{1}{2N}\sum_{ij}\bar{\boldsymbol{r}}_{ij}\bar{O}_{ij}\bar{\boldsymbol{F}}_{ij}\,|_{\boldsymbol{r}_i=\boldsymbol{r}}\,. \quad (33)\end{aligned}$$

Here, τ_I is the inertial relaxation time and τ_D is the relaxation time due to diffusion. Following equation (3), we impose a force balance in the limit of $t \gg \frac{\tau_I}{\tau_D}$. The stresses are computed using equation (33), with the differential operator truncated to the 1st order approximation, i.e. with $O_{ij} = 1$. This leads to equation (24).

References

1 V. R. Muzykantov, R. Radhakrishnan and D. M. Eckmann, *Current Drug Metabolism*, 2012, **13**, 70–81.

2 P. S. Ayyaswamy, V. Muzykantov, D. M. Eckmann and R. Radhakrishnan, *Journal of Nanotechnology in Engineering and Medicine*, 2013, **4**, 011001.

3 T. N. Swaminathan, J. Liu, U. Balakrishnan, P. S. Ayyaswamy, R. Radhakrishnan and D. M. Eckmann, *IUBMB Life*, 2011, **63**, 640–647.

4 J. A. Champion and S. Mitragotri, *Pharmaceutical research*, 2009, **26**, 244–249.

5 Y. Geng, P. Dalhaimer, S. Cai, R. Tsai, M. Tewari, T. Minko and D. E. Discher, *Nat Nano*, 2007, **2**, 249–255.

6 P. Kolhar, A. C. Anselmo, V. Gupta, K. Pant, B. Prabhakarpandian, E. Ruoslahti and S. Mitragotri, *Proceedings of the National Academy of Sciences*, 2013, **110**, 10753–10758.

7 A. Miller, *Current Medicinal Chemistry*, 2003, **10**, 1195–1211.

8 M. Malmsten, *Soft Matter*, 2006, **2**, 760–769.

9 D. C. Drummond, M. Zignani and J.-C. Leroux, *Progress in Lipid Research*, 2000, **39**, 409 – 460.

10 F. Ahmed, R. I. Pakunlu, A. Brannan, F. Bates, T. Minko and D. E. Discher, *Journal of Controlled Release*, 2006, **116**, 150 – 158.

11 M. Coll Ferrer, S. Dastgheyb, N. J. Hickok, D. M. Eckmann and R. J. Composto, *Acta Biomaterialia*, 2014, **10**, 2105 – 2111.

12 A. Conway, T. Vazin, D. P. Spelke, N. A. Rode, K. E. Healy, R. S. Kane and D. V. Schaffer, *Nat Nano*, 2013, **8**, 831–838.

13 D. M. Eckmann, R. J. Composto, A. Tsourkas and V. R. Muzykantov, *J. Mater. Chem. B*, 2014, **2**, 8085–8097.

14 J. Li and P. Yao, *Langmuir*, 2009, **25**, 6385–6391.

15 M. C. C. Ferrer, V. V. Shuvaev, B. J. Zern, R. J. Composto, V. R. Muzykantov and D. M. Eckmann, *PloS one*, 2014, **9**, e102329.

16 M. Coll Ferrer, J. Ferrier, Robert C., D. M. Eckmann and R. J. Composto, *Journal of Nanoparticle Research*, 2012, **15**, 1 – 7.

17 G. S. Grest and K. Kremer, *Phys. Rev. A*, 1986, **33**, 3628–3631.

18 G. S. Grest, K. Kremer and T. A. Witten, *Macromolecules*, 1987, **20**, 1376–1383.

19 J. J. Prentis, *The Journal of Chemical Physics*, 1982, **76**, 1574–1583.

20 M. Ripoll, R. G. Winkler and G. Gompper, *Phys. Rev. Lett.*, 2006, **96**, 188302.

21 S. P. Singh, A. Chatterji, G. Gompper and R. G. Winkler, *Macromolecules*, 2013, **46**, 8026–8036.

22 D. R. Foss and J. F. Brady, *Journal of Fluid Mechanics*, 2000, **407**, 167–200.

23 J. S. Hur, E. S. G. Shaqfeh and R. G. Larson, *Journal of Rheology (1978-present)*, 2000, **44**, 713–742.

24 D. Petera and M. Muthukumar, *The Journal of Chemical Physics*, 1999, **111**, 7614–7623.

25 C. M. Schroeder, E. S. G. Shaqfeh and S. Chu, *Macromolecules*, 2004, **37**, 9242–9256.

26 C.-C. Hsieh, L. Li and R. G. Larson, *Journal of Non-Newtonian Fluid Mechanics*, 2003, **113**, 147 – 191.

27 R. M. Jendrejack, J. J. de Pablo and M. D. Graham, *The Journal of Chemical Physics*, 2002, **116**, 7752–7759.

28 C. W. J. Beenakker, *The Journal of Chemical Physics*, 1986, **85**, 1581–1582.

29 Y. Liu, R. Lipowsky and R. Dimova, *Langmuir*, 2012, **28**, 3831–3839.

30 R. Pelton, J. Zhang, N. Chen and A. Moghaddamzadeh, *Tappi Journal*, 2003, **2**, 15–18.

31 K. Beers, *Numerical methods for chemical engineering applications in Matlab*, Cambridge University Press, Cambridge New York, 2007.

32 D. L. Ermak and J. A. McCammon, *The Journal of Chemical Physics*, 1978, **69**, 1352–1360.

33 J. D. Weeks, D. Chandler and H. C. Andersen, *The Journal of Chemical Physics*, 1971, **54**, 5237–5247.

34 J. Rotne and S. Prager, *The Journal of Chemical Physics*, 1969, **50**, 4831–4837.

35 H. Yamakawa, *The Journal of Chemical Physics*, 1970, **53**, 436–443.

36 T. Zhou and S. B. Chen, *The Journal of Chemical Physics*, 2006, **124**, 034904.

37 C. H. Rycroft, *Chaos: An Interdisciplinary Journal of Nonlinear Science*, 2009, **19**, 041111.

38 T. A. Witten, P. A. Pincus and M. E. Cates, *EPL (Europhysics Letters)*, 1986, **2**, 137.

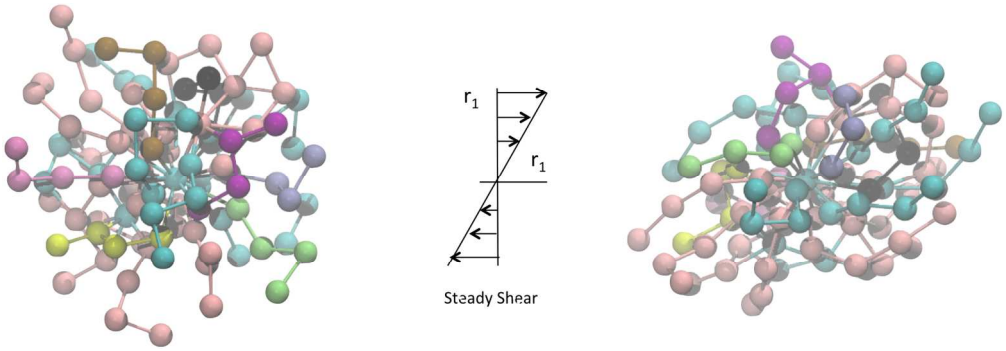

Hydrodynamic deformation of polymeric nanocarriers
600x207mm (72 x 72 DPI)